

Article

Synthesis and Broadband Spectra Photocatalytic Properties of $\text{Bi}_2\text{O}_2(\text{CO}_3)_{1-x}\text{S}_x$

Junping Ding ^{1,2}, Huanchun Wang ^{1,3}, Haomin Xu ¹, Lina Qiao ¹, Yidong Luo ¹, Yuanhua Lin ^{1,*} and Cewen Nan ¹

¹ State Key Laboratory of New Ceramics and Fine Processing, School of Materials Science and Engineering, Tsinghua University, Beijing 100084, China; djp15@mails.tsinghua.edu.cn (J.D.); huanchunwang@163.com (H.W.); xuhm13@mails.tsinghua.edu.cn (H.X.); qln13@mails.tsinghua.edu.cn (L.Q.); ydluozd@163.com (Y.L.); cwnan@mail.tsinghua.edu.cn (C.N.)

² China Astronaut Research and Training Center, Beijing 100094, China

³ High-Tech Institute of Xi'an, Xi'an 710025, China

* Correspondence: linyh@mail.tsinghua.edu.cn; Tel.: +86-10-6277-3741

Received: 31 March 2018; Accepted: 3 May 2018; Published: 14 May 2018



Abstract: High efficiency photocatalyst $\text{Bi}_2\text{O}_2(\text{CO}_3)_{1-x}\text{S}_x$ was synthesized conveniently with chemical bath precipitation using $\text{Bi}_2\text{O}_2\text{CO}_3$ as the precursor. The microstructures of the samples are systematically characterized by X-ray diffraction (XRD), scanning electron microscopy (SEM), high resolution transmission electron microscopy (HRTEM), X-ray photoelectron spectroscopy (XPS), ultraviolet photoelectron spectroscopy (UPS) and UV-Vis spectroscopy; the optical and photocatalytic properties are carefully tested as well. The content of S, which was tuned through the controlling of the precipitation process, was verified to have an intense effect over the photocatalytic properties. A nearly saturated S ratio and the best photocatalytic performance were observed in specimens with the most S content. Our study reveals that, with negligible influence of the morphology and crystal structure, $\text{Bi}_2\text{O}_2(\text{CO}_3)_{1-x}\text{S}_x$ possessed a broadened optical absorption region from ultraviolet to visible light, and enhanced photocatalytic activity in comparison to precursor $\text{Bi}_2\text{O}_2\text{CO}_3$ in photocatalytic degradation of Congo Red aqueous solution.

Keywords: $\text{Bi}_2\text{O}_2\text{CO}_3$; $\text{Bi}_2\text{O}_2(\text{CO}_3)_{1-x}\text{S}_x$; broadband spectra; photocatalysis

1. Introduction

Semiconductor photocatalysis has attracted increasing attention because of the capability of harvesting the solar energy to eliminate environmental pollutants [1–7]. Among various semiconductors, some Aurivillius type bismuth-based oxide semiconductor materials such as BiOX ($X = \text{Cl}, \text{Br}, \text{I}$), BiVO_4 and Bi_2WO_6 have been widely used in photocatalysis [8–14].

Bismuth-based layered-structure compounds have a unique crystal structure and band structure. Hybridisation between 6s electrons of Bi and 2p electrons of O form chemical bonds which are stronger than those between Bi and other nonmetallic atoms (such as chalcogen), leading to a particularly stable $(\text{Bi-O})^+$ layer. A series of Bi-based layered-structural photocatalytic materials of various band gap widths from 3.2 eV (e.g., BiOCl [15]) to 1.12–1.5 eV (e.g., $\text{Bi}_2\text{O}_2\text{S}$ [16,17]) can be obtained by combining the $(\text{Bi-O})^+$ layer with different anion layers. In addition, p-type (BiCuSO or the like) or n-type ($\text{Bi}_2\text{O}_2\text{CO}_3$, etc.) semiconductor materials can be obtained by adjusting the anion layer. Therefore, the different Bi-based oxide composite structure can not only control and broaden the range of light absorption of the catalyst, but also may form a hetero structure such as p-n junction.

Recently, $\text{Bi}_2\text{O}_2\text{CO}_3$, which is a member of the Aurivillius-type family and composed of $[\text{Bi}_2\text{O}_2]^{2+}$ layers interleaved by CO_3^{2-} layers [18,19], has attracted growing concern because of its photocatalytic

ability to decompose organic pollutants in liquid phase and NO in gaseous phase [20–22]. Its unique layered structure, resulting in a large internal electrostatic field and asymmetric polarization effect, contributes to the separation of photogenerated electron-hole pairs [23,24]. However, the application of $\text{Bi}_2\text{O}_2\text{CO}_3$ in photodegradation is strongly limited by its large band gap (~ 3.3 eV). To overcome this limitation, many methods have been developed, such as the fabrication of heterojunctions such as $\text{BiVO}_4/\text{Bi}_2\text{O}_2\text{CO}_3$, $\text{Bi}_2\text{S}_3/\text{Bi}_2\text{O}_3/\text{Bi}_2\text{O}_2\text{CO}_3$ [25–27], noble metal deposition [28], elemental doping [29], and morphological modulation [30].

In this paper, we have synthesized S-doped $\text{Bi}_2\text{O}_2(\text{CO}_3)_{1-x}\text{S}_x$ by chemical bath precipitation, using $\text{Bi}_2\text{O}_2\text{CO}_3$ as the precursor, through the controlling of the precipitation process to have an intense effect over the photocatalytic properties. A nearly saturated S ratio and the best photocatalytic performance were observed in specimens with the most S content. With a negligible influence of the morphology and crystal structure, the optical absorption of $\text{Bi}_2\text{O}_3\text{CO}_3$ was extended from the ultraviolet (UV) to the visible region. The photocatalytic degradation of Congo Red showed that $\text{Bi}_2\text{O}_2(\text{CO}_3)_{1-x}\text{S}_x$ exhibited enhanced photoactivity in comparison to the precursor powder.

2. Results and Discussion

2.1. Synthetic $\text{Bi}_2\text{O}_2(\text{CO}_3)_{1-x}\text{S}_x$

Figure 1 shows the XRD(X-ray diffraction) pattern of the $\text{Bi}_2\text{O}_2\text{CO}_3$ powder prepared by hydrothermal method, together with a reference pattern of tetragonal $\text{Bi}_2\text{O}_2\text{CO}_3$ (JCPDS: 41–1488). No second phase can be found, and the sharp peaks indicate well-developed crystallinity. The preparation process of $\text{Bi}_2\text{O}_2\text{CO}_3$ can be summarized in Equations (1)–(3). CO_3^{2-} forms through a hydrolysis reaction between $(\text{NH}_2)_2\text{CO}$ and H_2O . Bi_2O_3 is also strongly hydrolyzed with water to produce $(\text{Bi}_2\text{O}_2)^{2+}$. The produced $(\text{Bi}_2\text{O}_2)^{2+}$ and CO_3^{2-} then react to generate $\text{Bi}_2\text{O}_2\text{CO}_3$.

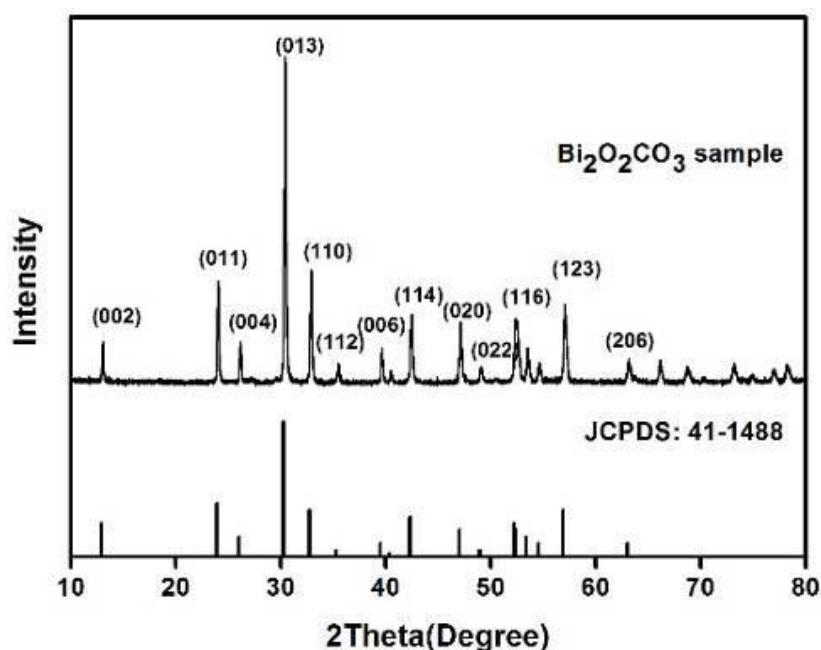
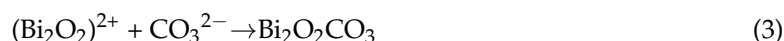


Figure 1. XRD pattern of hydrothermally synthesized $\text{Bi}_2\text{O}_2\text{CO}_3$.

In addition, the percentage of crystallinity and the BET (Brunauer–Emmett–Teller) specific surface area of the samples with a S:Bi₂O₂CO₃ ratio *n* equals to 0, 0.01, 0.02, 0.05, 0.10 and 0.20 (marked as M0, M1, M2, M5, M10 and M20, respectively) are shown in Table 1. There are no significant changes in their percentage of crystallinity, while samples of M5 and M10 display larger specific surface areas than that of other samples, which could lead to the exposure of more active sites for the photocatalytic experiment. The scanning electron microscopy (SEM) photograph and the high resolution transmission electron microscopy (HRTEM) images of the powder are shown in Figures 2 and 3. The morphology of the particles are nano-sized flakes of about 60–80 nm in thickness. In addition, the crystallinity of different samples calculated from the XRD results shows that S doping introduced defects in the Bi₂O₂CO₃ and thus caused crystallinity change.

Table 1. Surface area and percentage of crystallinity of the Bi₂O₂CO₃ and M1–M20 powders.

	M0	M1	M2	M5	M10	M20
Surface area (m ² /g)	0.917	0.973	0.980	1.666	1.823	0.966
Percentage of crystallinity (%)	–	74.43 ± 0.96	65.62 ± 0.61	74.14 ± 0.88	77.31 ± 0.75	79.87 ± 1.75

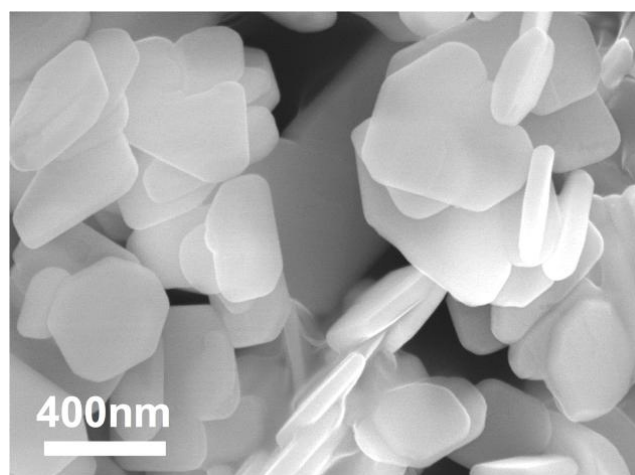


Figure 2. SEM photograph of hydrothermal synthesised Bi₂O₂CO₃.

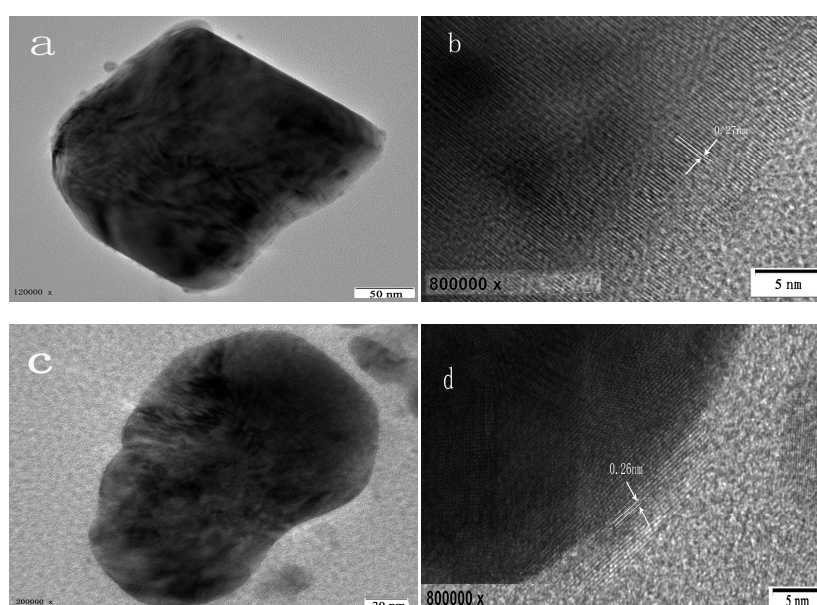


Figure 3. HRTEM images of M0 (a); (b) and M20 (c); (d).

The XRD patterns of the samples prepared by the Na_2S chemical bath precipitation are shown in Figure 4a. All diffraction peaks are consistent with $\text{Bi}_2\text{O}_2\text{CO}_3$, indicating that chemical bath precipitation did not introduce a significant second phase. The intensity of the diffraction peak does not obviously decrease, and the products still have good crystallinity. The position of the (013) diffraction peak for different samples are shown in Figure 4b. No obvious influence of Na_2S chemical precipitation on the crystal structure of $\text{Bi}_2\text{O}_2\text{CO}_3$ can be found because the position of the peak (013) did not show an apparent shift according to XRD results.

X-ray photoelectron spectroscopy (XPS) was utilized to obtain insights into the valence states and surface chemical compositions details of $\text{Bi}_2\text{O}_2(\text{CO}_3)_{1-x}\text{S}_x$. As shown in Figure 5a, the XPS spectrum of Bi-4f shows two peaks at 159.05 and 164.35 eV, which belong to Bi-4f_{7/2} and Bi-4f_{5/2} energy levels, respectively. These two peaks are characteristic features of trivalent Bi in $\text{Bi}_2\text{O}_2(\text{CO}_3)_{1-x}\text{S}_x$ [31]. The two peaks at 284.7 eV and 288.8 eV in Figure 5b show that the existence form of C is CO_3^{2-} [32]. In Figure 5c, the two peaks are at 530.5 eV and 531 eV, which belong to O energy levels in B-O and CO_3^{2-} , respectively [33]. In Figure 5d, the peak of S-2p is at the range of 158–166 eV, which shows that the existence form of S is S^{2-} [17]. On the other hand, the Bi-4f peak of M20 apparently shifts compared to M0 (Figure 5a), which proves that S takes place of CO_3^{2-} partially [34].

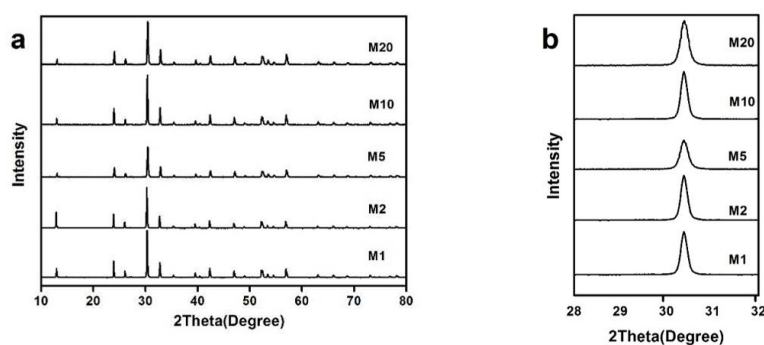


Figure 4. (a) XRD patterns of $\text{Bi}_2\text{O}_2(\text{CO}_3)_{1-x}\text{S}_x$ prepared by chemical bath precipitation; (b) the position of the (013) diffraction.

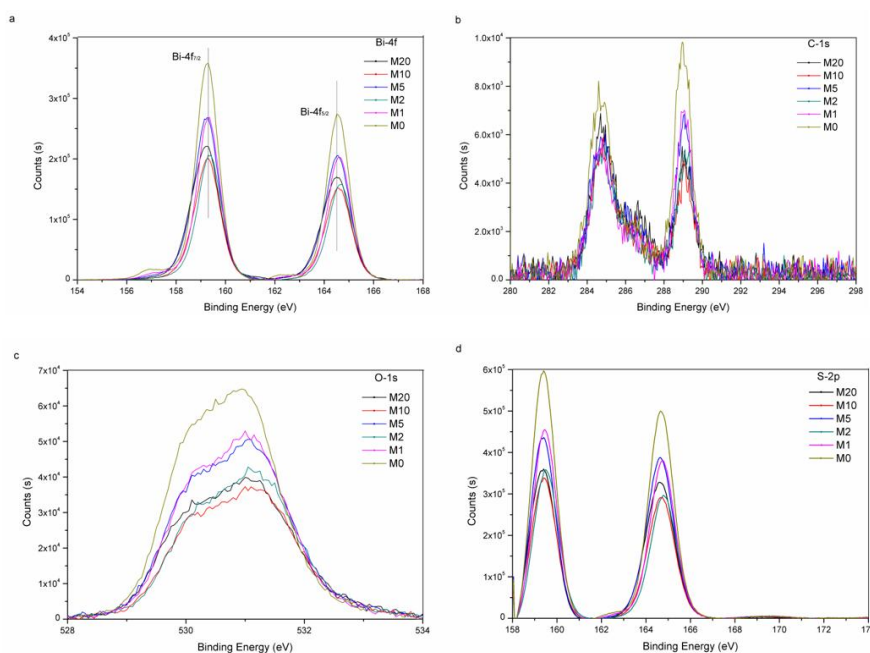


Figure 5. XPS spectra of M0, M1, M2, M5, M10 and M20, Bi-4f (a); C-1s (b); O-1s (c); and S-2p (d).

Although Na_2S chemical precipitation had no obvious influence on the crystal structure of $\text{Bi}_2\text{O}_2\text{CO}_3$, the powder color was changed from white to yellow, and the color became darker as S: $\text{Bi}_2\text{O}_2\text{CO}_3$ molar ratio n increased. The UV-Vis diffuse reflectance spectra are shown in Figure 6. $\text{Bi}_2\text{O}_2\text{CO}_3$ has a strong absorption of UV light with wavelengths less than 360 nm and weak absorption to 400 nm~500 nm-wavelength-visible light due to defects and oxygen vacancy, which also explained the fact that $\text{Bi}_2\text{O}_2\text{CO}_3$ could display visible light photocatalytic activity with the bandgap of 3.2 eV. With the introduction of S, the light absorption behaviour was significantly changed from M1 to M20. In particular, the absorption of visible light increased by about one order of magnitude. The band gap of $\text{Bi}_2\text{O}_2\text{CO}_3$ without sulfur is fitted as 3.27 eV, and the introduction of S leads to the emergence of a narrow band gap by lowering the conduction band position and meanwhile generating impurity levels [35,36]. The adsorption edge is around 380 nm. With the increase of S content, defects and oxygen vacancies increase, possibly due to point defects, and the fitted narrow band gap decreases from 3.25 to 2.20 eV. Energy levels of the valence band maximum (E_{VB}) were measured by the ultraviolet photoelectron spectrometer at UV intensity 500 nW and energy levels of the conduction band minimum (E_{CB}) were calculated by the bandgap. As shown in Figure 7, valence band edge position and conduction band edge position become more negative after the incorporation of sulfur into $\text{Bi}_2\text{O}_2\text{CO}_3$.

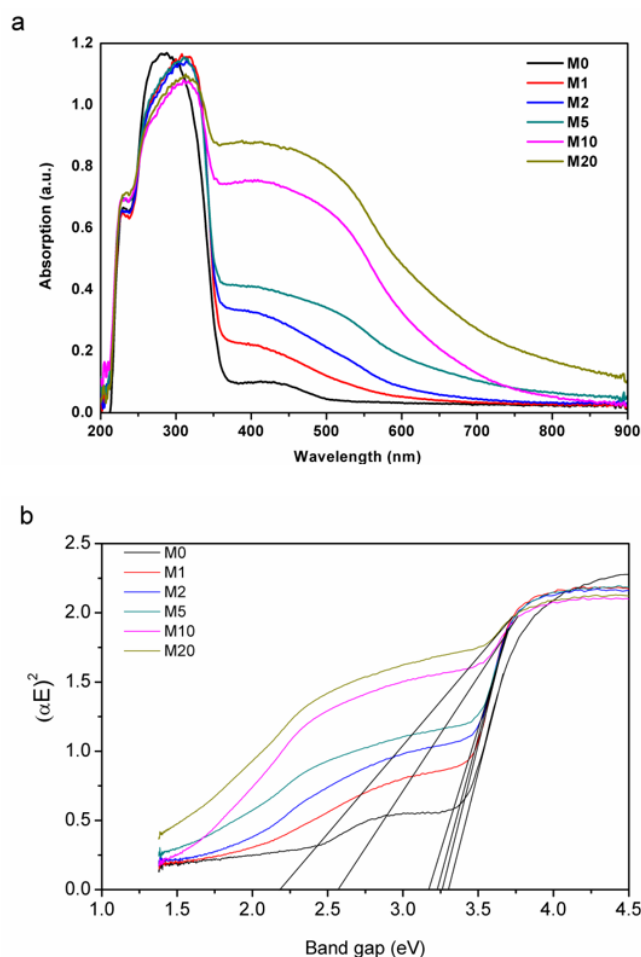


Figure 6. (a) UV-Vis diffuse reflectance spectra of the synthesized $\text{Bi}_2\text{O}_2(\text{CO}_3)_{1-x}\text{S}_x$; (b) band gap fitting with K-M relation.

The SEM observation showed that chemical bath treatment had little influence on the morphology of the $\text{Bi}_2\text{O}_2\text{CO}_3$ particles. EDS (energy dispersive spectroscopy) elemental mapping in Figure 8 revealed the homogeneous distribution of S on the particle surface, and no obvious segregation and

aggregation can be seen among the particles. The quantitative elemental analysis results are shown in Table 2. The S content in samples M1~M20 increases with the increase of S: $\text{Bi}_2\text{O}_2\text{CO}_3$ molar ratio n , but the S atom percentage (referring to Bi-content) is obviously smaller than n and becomes stable as n is greater than 0.10. This is consistent with the calculations about the surface adsorption of $\text{Bi}_2\text{O}_2\text{CO}_3$ by Chang [34], who suggested that S^{2-} can be adsorbed in the oxygen vacancy of the (001) plane via the chemical bonding and reduce the surface energy. The calculation of the density of states near the Fermi level shows that the doping of S can introduce a new energy level in the energy band and reduce the band gap. The electron state density near the Fermi surface is more diffusive, which favours the migration of electrons and therefore improves the photocatalytic performance.

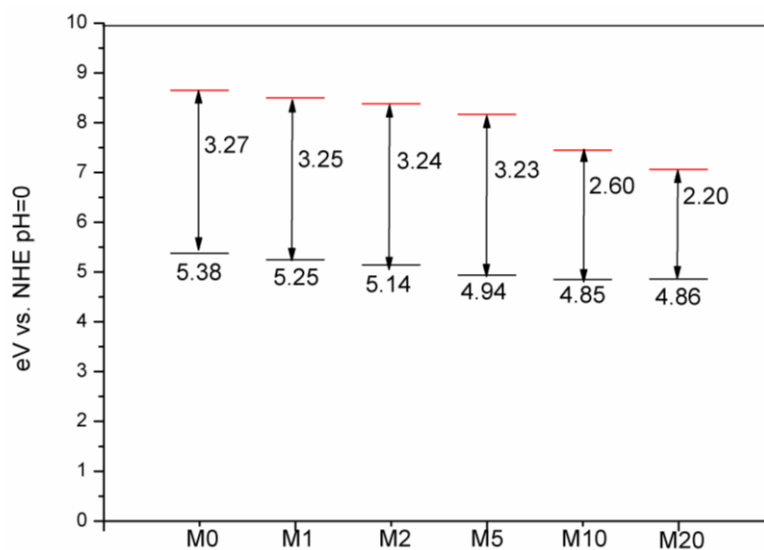


Figure 7. Energy levels of the conduction band minimum (E_{CB} , red) and the valence band maximum (E_{VB} , black) calculated at theoretical pH = 0 (V is voltage; NHE is normalhydrogen electrode potential).

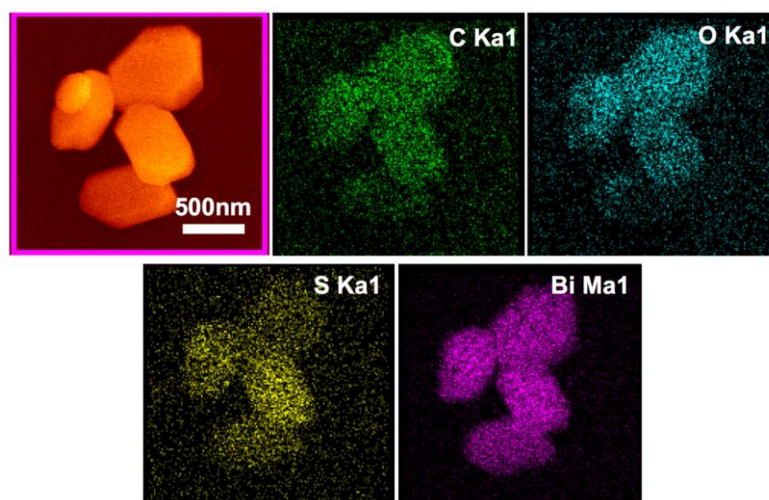


Figure 8. EDS element mapping details of M20 particles.

Table 2. EDS quantitative results of the M0~M20 powders.

	M0	M1	M2	M5	M10	M20
C K	43.78	43.88	43.90	44.11	44.30	44.41
O K	45.53	45.30	45.30	45.27	45.17	45.10
S K	–	0.04	0.06	0.11	0.24	0.29
Bi M	10.69	10.78	10.74	10.51	10.29	10.20
<i>x</i>	0	0.007	0.011	0.021	0.047	0.057

2.2. Ultraviolet-Visible Light Photocatalytic Properties of $\text{Bi}_2\text{O}_2(\text{CO}_3)_{1-x}\text{S}_x$

The photocatalytic activity of $\text{Bi}_2\text{O}_2(\text{CO}_3)_{1-x}\text{S}_x$ was characterised by photocatalytic degradation of Congo Red. As is shown in Figure 9, the introduction of S could improve the photocatalytic activity of $\text{Bi}_2\text{O}_2\text{CO}_3$ under visible light and UV light. We measured the dye adsorption before switching on the light and normalized the concentrations, which made initial values of c/c_0 equal to 1 for all samples. The operation temperature used was around 0 °C. With pure $\text{Bi}_2\text{O}_2\text{CO}_3$, the Congo Red degrades by 41.6% under the irradiation of visible light for 3h, and by 46.1% under that of UV light, respectively. With the increase of molar ratio of S: $\text{Bi}_2\text{O}_2\text{CO}_3$ from 0.01 to 0.1, the degradation rate increases to 64.2% and 70.1%, respectively. The further increase of *n*, however, cannot further remarkably increase the degradation rate. At the highest molar ratio of S(0.2), the photocatalytic activity of Congo Red was 65.3% and 71.4%, respectively, which was 1.57 and 1.55 times higher than that of $\text{Bi}_2\text{O}_2\text{CO}_3$, respectively. The photo-degradation behavior of CR by use of $\text{Bi}_2\text{O}_2(\text{CO}_3)_{1-x}\text{S}_x$ obeys pseudo-first-order kinetics. This can be fitted by the Langmuir–Hinshelwood model of $\ln(C_0/C) = kt + A$, where *k* is the reaction rate constant, *t* is the degradation time and the intercept *A* is the initial value of $\ln(C_0/C)$, which means the dark adsorption of substrates. The *k* value of M1, M2, M5, M10 and M20 under UV light is $4.3 \times 10^{-3} \text{ min}^{-1}$, $5.5 \times 10^{-3} \text{ min}^{-1}$, $6.1 \times 10^{-3} \text{ min}^{-1}$, $6.8 \times 10^{-3} \text{ min}^{-1}$ and $6.9 \times 10^{-3} \text{ min}^{-1}$, respectively. The *k* value under visible light is $3.0 \times 10^{-3} \text{ min}^{-1}$, $3.5 \times 10^{-3} \text{ min}^{-1}$, $4.7 \times 10^{-3} \text{ min}^{-1}$, $5.5 \times 10^{-3} \text{ min}^{-1}$ and $5.9 \times 10^{-3} \text{ min}^{-1}$, respectively. The strong visible light sensitivity indicates higher utilization efficiency of solar light, making $\text{Bi}_2\text{O}_2(\text{CO}_3)_{1-x}\text{S}_x$ a superior photocatalyst than the commercial P25 TiO_2 , which has been reported to be hardly able to respond to visible light [37,38].

Chang's theoretical calculations [34] suggest that S can be easily captured and adsorbed by oxygen vacancies on the surface of $\text{Bi}_2\text{O}_2\text{CO}_3$ as formed S^{2-} can partially substitute CO_3^{2-} without forming a second phase, introducing a bend built-in electric field. At the same time, their experiments also confirmed that $\text{Bi}_2\text{O}_2(\text{CO}_3)_{1-x}\text{S}_x$ had higher conductivity and better carrier transport performance. The photoluminescence (PL) spectra of different S-substituted $\text{Bi}_2\text{O}_2(\text{CO}_3)_{1-x}\text{S}_x$ (Figure 10) show that samples M10 and M20 displayed weaker electron holes and recombination, indicating that the introduction of S can effectively suppress the carrier recombination. The stronger light absorption contributed by the smaller band gap means more photo-induced electron hole generation, and those electron holes showed better separation according to PL spectra. It is worthnoting that M20 has a stronger light absorption and smaller bandgap than that of M10, but that they present nearly the same photocatalytic activity, which may be caused by the smaller specific surface area (Table 1) and slightly weaker separation (Figure 10) of M20. Thus, all the three factors helped enhance the photocatalytic performance of $\text{Bi}_2\text{O}_2\text{CO}_3$ in our samples under UV and visible light irradiation.

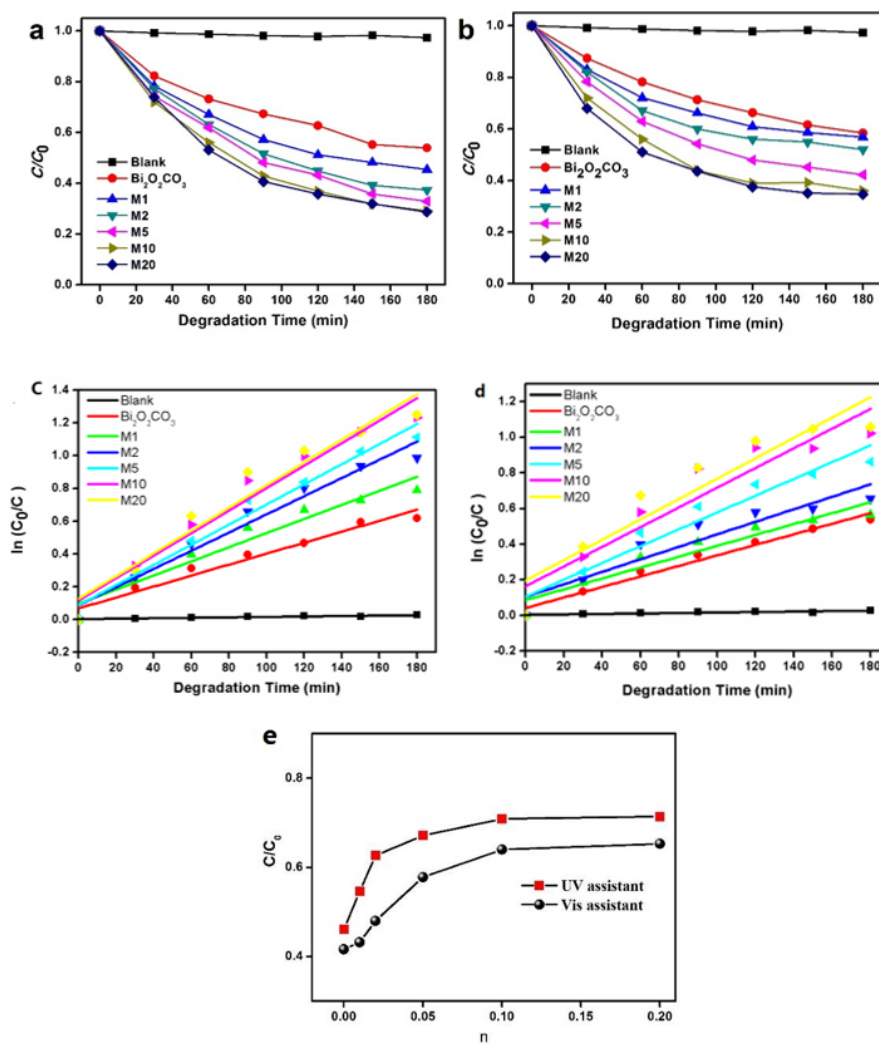


Figure 9. Degradation of Congo Red under the irradiation of (a,c) UV, and (b,d) visible light, with $\text{Bi}_2\text{O}_2(\text{CO}_3)_{1-x}\text{S}_x$; (e) the degradation rate as a function of n ($=\text{S}:\text{Bi}_2\text{O}_2\text{CO}_3$).

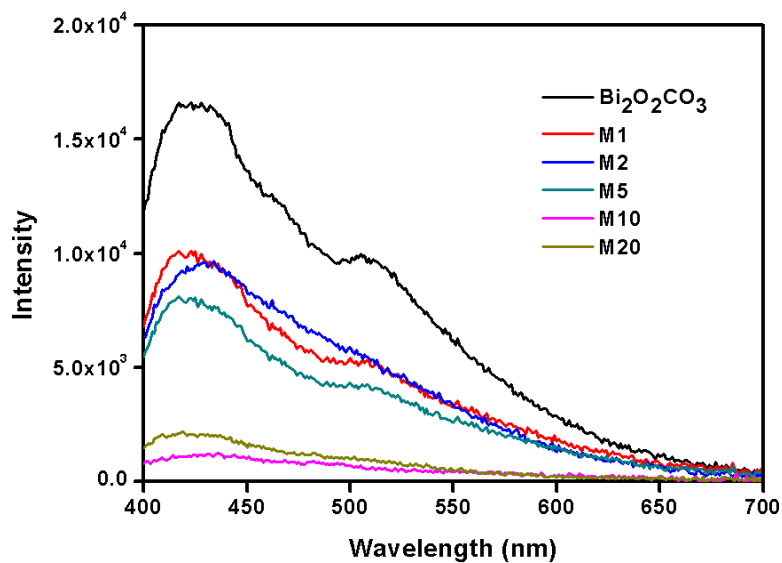


Figure 10. Photoluminescence spectra of $\text{Bi}_2\text{O}_2(\text{CO}_3)_{1-x}\text{S}_x$.

3. Materials and Methods

3.1. Preparation of the Precursor Powder $\text{Bi}_2\text{O}_2\text{CO}_3$ via Hydrothermal Method

Three grams of urea ($\geq 99.0\%$, Beijing Modern Orient Fine Chemistry Co. Ltd., Beijing, China) was dissolved in 60 mL of deionized water in a Teflon hydrothermal tank. 4.65 g Bi_2O_3 powder (99.99%, Aladdin Industrial Corporation, Shanghai, China) was then introduced into the solution. The hydrothermal tank was then tightly closed and kept in an oven at 180 °C for 12 h. After cooling down to room temperature, the precipitate was separated and washed with deionized water and ethanol several times and then dried in the oven at 70 °C.

3.2. Preparation of $\text{Bi}_2\text{O}_2(\text{CO}_3)_{1-x}\text{S}_x$ by Chemical Bath Precipitation

Five suspensions of $\text{Bi}_2\text{O}_2\text{CO}_3$ were prepared, each by dispersing 2.04 g of $\text{Bi}_2\text{O}_2\text{CO}_3$ powder in 50 mL of deionized water with the help of ultrasonic stirring for 10 min. A certain amount (S: $\text{Bi}_2\text{O}_2\text{CO}_3$ ratio n , equals to 0.01, 0.02, 0.05, 0.10 and 0.20, respectively) of 0.5 mol/L Na_2S ($\geq 98.0\%$, Shanghai Tongya Chemical Technology Co. Ltd., Shanghai, China) solution was introduced into the respective suspensions. After 8 h of further magnetic stirring at room temperature, the precipitates were separated and washed several times with deionized water and ethanol and dried at 70 °C. As-treated powders were numbered as M1, M2, M5, M10 and M20, respectively.

3.3. Characterization

Powder X-ray diffraction (XRD) was completed on a diffractometer (D8-Advance, Bruker, Billerica, MA, USA) using monochromatized $\text{Cu K}\alpha$ ($\lambda = 0.15418$ nm) radiation with scanning speed of 3°/min. The morphology of the samples were carried out on a scanning electron microscope (JSM-7001F, JEOL, Tokyo, Japan) operating at a 5 kV and a field emission electron microscope (JEM-2100F, JEOL). The surface areas of specimens were tested on a automated gas sorption analyser (Quantachrome, autosorb iQ2). The X-ray photoelectron spectroscopic (XPS) measurements were performed on a Thermo Fisher ESCALAB 250Xi instrument. A UV-Vis-NIR spectrometer (Lambda 950, PerkinElmer, Waltham, MA, USA) was used to measure UV-Vis diffuse reflectance spectra (DRS). Energy levels of the valence band maximum (E_{VB}) were measured by the ultraviolet photoelectron spectrometer (AC-2, RIKEN KEIKI, Tokyo, Japan).

3.4. Photocatalytic Test

The photocatalytic activity of the prepared $\text{Bi}_2\text{O}_2(\text{CO}_3)_{1-x}\text{S}_x$ powder samples was evaluated by photodegrading Congo Red (CR, 100 mg/L) aqueous solution. The reason we chose this concentration is because it is proper to evaluate the change of the color. 0.16 g photocatalyst powder specimen was dispersed into 80 mL CR solution and stirred in the dark for 2 h to reach the adsorption–desorption equilibrium between the photocatalysts and organic dye molecules. Magnetic stirring and a cooling-water bath were held continuously to prevent thermal effect during the degradation process and to keep the uniformity. A 5W LED with emission wavelength of 365 ± 5 nm and a 300 W xenon lamp with 420 nm cut-off filters were used as the UV (365–800 nm) and visible light sources (420–800 nm), respectively. The incident light source was placed above the aqueous solution vertically, and the illumination intensity for UV and visible lights at upper surface of the solution were about 78 mW/cm² and 132 mW/cm². The photocatalytic processes were conducted under constant temperature, using ice water to cool the system. At the end of regular time intervals, 3 mL suspension was collected and centrifuged, and the residual CR concentration in the supernatant fluid was analyzed by UV-vis spectrophotometer (UV–3100, Hitachi, Tokyo, Japan).

4. Conclusions

AnNa₂S chemical bath treatment of Bi₂O₂CO₃ did not generate a second phase. It is shown that the introduction of S can effectively broaden the optical absorption range, although it does not apparently change the crystal structure of Bi₂O₂CO₃. The electrons at the top of the valence band in Bi₂O₂(CO₃)_{1-x}S_x can be excited by shorter wavelengths of sunlight, forming photo-generated electron-hole pairs. This may be due to the formation of chemical bonds between the S²⁻ and vacancies on the surface of Bi₂O₂CO₃ crystal, which can affect the surface properties.

Bi₂O₂(CO₃)_{1-x}S_x can improve the catalytic performance of visible and UV regions to a certain extent by the introduction of S in Bi₂O₂CO₃ by chemical bath. This is because the introduction of S can effectively suppress the carrier recombination and improve the carrier transport performance. However, S can be introduced only into the surface of Bi₂O₂CO₃ by chemical bath at room temperature, and the improvement of catalytic performance is limited.

Author Contributions: Y.L. and J.D. designed the project; J.D. conducted the most experiments; L.Q. and H.X. performed part of the experiments; J.D. and H.W. together wrote and revised the manuscript with input from all the authors. C.N. and Y.L. took part in discussing and the revision of the manuscript.

Acknowledgments: This work was supported by National Natural Science Foundation of China (no. 51221291, no. 51328203 and 51532003).

Conflicts of Interest: The authors declare no conflict of interest.

References

1. Tong, H.; Ouyang, S.; Bi, Y.; Umezawa, N.; Oshikiri, M.; Ye, J. Nano-photocatalytic materials: Possibilities and challenges. *Adv. Mater.* **2012**, *24*, 229–251. [[CrossRef](#)] [[PubMed](#)]
2. Wang, P.; Huang, B.B.; Dai, Y.; Whangbo, M.H. Plasmonic photocatalysts: Harvesting visible light with noble metal nanoparticles. *Phys. Chem. Chem.* **2012**, *14*, 9813–9825. [[CrossRef](#)] [[PubMed](#)]
3. Wang, H.L.; Zhang, L.S.; Chen, Z.G.; Hu, J.Q.; Li, S.J.; Wang, Z.H.; Liu, J.S.; Wang, X.C. Semiconductor heterojunction photocatalysts: Design, construction, and photocatalytic performances. *Chem. Soc. Rev.* **2014**, *43*, 5234–5244. [[CrossRef](#)] [[PubMed](#)]
4. Moniz, S.J.A.; Shevlin, S.A.; Martin, D.J.; Guo, Z.X.; Tang, J.W. Visible-light driven heterojunction photocatalysts for water splitting—A critical review. *Energy Environ. Sci.* **2015**, *8*, 731–759. [[CrossRef](#)]
5. Yu, J.G.; Low, J.X.; Xiao, W.; Zhou, P.; Jaroniec, M. Enhanced photocatalytic CO₂-reduction activity of anatase TiO₂ by coexposed {001} and {101} facets. *J. Am. Chem. Soc.* **2014**, *136*, 8839–8842. [[CrossRef](#)] [[PubMed](#)]
6. Chava, R.K.; Do, J.Y.; Kang, M. Hydrothermal growth of two dimensional hierarchical MoS₂ nanospheres on one dimensional CdS nanorods for high performance and stable visible photocatalytic H₂ evolution. *Appl. Surf. Sci.* **2018**, *433*, 240–248. [[CrossRef](#)]
7. Chava, R.K.; Do, J.Y.; Kang, M. Fabrication of CdS-Ag₃PO₄ heteronanostructures for improved visible photocatalytic hydrogen evolution. *J. Alloys Compd.* **2017**, *727*, 86–93. [[CrossRef](#)]
8. Ye, L.Q.; Su, Y.R.; Jin, X.L.; Xie, H.Q.; Zhang, C. Recent advances in BiOX (X = Cl, Br and I) photocatalysts: Synthesis, modification, facet effects and mechanisms. *Environ. Sci. Nano* **2014**, *1*, 90–112. [[CrossRef](#)]
9. Xiao, X.; Liu, C.; Hu, R.; Zuo, X.; Nan, J.; Li, L.; Wang, L. Oxygen-rich bismuth oxyhalides: Generalized one-pot synthesis, band structures and visible light photocatalytic properties. *J. Mater. Chem.* **2012**, *22*, 22840–22843. [[CrossRef](#)]
10. Kim, T.W.; Choi, K.S. Nanoporous BiVO₄ photoanodes with dual-layer oxygen evolution catalysts for solar water splitting. *Science* **2014**, *343*, 990–994. [[CrossRef](#)] [[PubMed](#)]
11. Kudo, A.; Omori, K.; Kato, H. A novel aqueous process for preparation of crystal form-controlled and highly crystalline BiVO₄ powder from layered vanadates at room temperature and its photocatalytic and photophysical properties. *J. Am. Chem. Soc.* **2000**, *31*, 11459–11467. [[CrossRef](#)]
12. Zhou, L.; Jin, C.G.; Yu, Y.; Chi, F.L.; Ran, S.L.; Lv, Y.H. Molten salt synthesis of Bi₂WO₆ powders with enhanced visible-light induced photocatalytic activities. *J. Alloys Compd.* **2016**, *680*, 301–308. [[CrossRef](#)]

13. Zhang, J.; Huang, L.H.; Yang, L.X.; Lu, Z.D.; Wang, X.Y.; Xu, G.L.; Zhang, E.P.; Wang, H.B.; Kong, Z.; Xi, J.H.; et al. Controllable synthesis of Bi₂WO₆ (001)/TiO₂ (001) heterostructure with enhanced photocatalytic activity. *J. Alloys Compd.* **2016**, *676*, 37–45. [[CrossRef](#)]
14. Kalithasan, N.; Hari, C.B.; Rajesh, J.T. Photocatalytic efficiency of bismuth oxyhalide (Br, Cl and I) nanoplates for RhB dye degradation under LED irradiation. *J. Ind. Eng. Chem.* **2016**, *34*, 146–156.
15. Zhang, H.; Yang, Y.; Zhou, Z.; Zhao, Y.; Liu, L. Enhanced photocatalytic properties in BiOBr nanosheets with dominantly exposed (102) facets. *J. Phys. Chem. C* **2014**, *118*, 14662–14669. [[CrossRef](#)]
16. Zhang, X.; Liu, Y.; Zhang, G.; Wang, Y.; Zhang, H.; Huang, F. Thermal decomposition of bismuth oxysulfide from photoelectric Bi₂O₂S to Superconducting Bi₄O₄S₃. *ACS Appl. Mater. Interfaces* **2015**, *7*, 4442–4448. [[CrossRef](#)] [[PubMed](#)]
17. Pacquette, A.L.; Hagiwara, H.; Ishihara, T.; Gewirth, A.A. Fabrication of an oxysulfide of bismuth Bi₂O₂S and its photocatalytic activity in a Bi₂O₂S/In₂O₃ composite. *J. Photochem. Photobiol. A Chem.* **2014**, *277*, 27–36. [[CrossRef](#)]
18. Tsunoda, Y.; Sugimoto, W.; Sugahara, Y. Intercalation behavior of *n*-alkylamines into a protonated form of a layered perovskite derived from aurivillius phase Bi₂SrTa₂O₉. *Chem. Mater.* **2003**, *15*, 632–635. [[CrossRef](#)]
19. Huang, Y.; Wang, W.; Zhang, Q.; Cao, J.J.; Huang, R.J.; Ho, W.K.; Lee, S.C. In Situ fabrication of a-Bi₂O₃/(BiO)₂CO₃ nanoplate heterojunctions with tunable optical property and photocatalytic activity. *Sci. Rep.* **2016**, *6*, 23435. [[CrossRef](#)] [[PubMed](#)]
20. Ni, Z.L.; Sun, Y.J.; Zhang, Y.X.; Dong, F. Fabrication, modification and application of (BiO)₂CO₃-based photocatalysts: A review. *Appl. Surf. Sci.* **2016**, *365*, 314–335. [[CrossRef](#)]
21. Cheng, H.F.; Huang, B.B.; Yang, K.S.; Wang, Z.Y.; Qin, X.Y.; Zhang, X.Y.; Dai, Y. Facile template-free synthesis of Bi₂O₂CO₃ hierarchical microflowers and their associated photocatalytic activity. *J. Phys. Chem. C* **2010**, *11*, 2167–2173. [[CrossRef](#)] [[PubMed](#)]
22. Dong, F.; Xiong, T.; Sun, Y.J.; Huang, H.W.; Wu, Z.B. Synergistic integration of thermocatalysis and photocatalysis on black defective (BiO)₂CO₃ microspheres. *J. Mater. Chem. A* **2015**, *3*, 18466–18474. [[CrossRef](#)]
23. Huang, H.W.; Wang, J.J.; Dong, F.; Guo, Y.X.; Tian, N.; Zhang, Y.H.; Zhang, T.R. Highly Efficient Bi₂O₂CO₃ Single-Crystal Lamellas with Dominantly Exposed {001} Facets. *Cryst. Growth Des.* **2015**, *15*, 534–537. [[CrossRef](#)]
24. Huang, H.W.; Tian, N.; Jin, S.F.; Zhang, Y.H.; Wang, S.B. Syntheses, characterization and nonlinear optical properties of a bismuth subcarbonate Bi₂O₂CO₃. *Solid State Sci.* **2014**, *30*, 1–5. [[CrossRef](#)]
25. Madhusudan, P.; Ran, J.R.; Zhang, J.; Yu, J.G.; Liu, G. Novel urea assisted hydrothermal synthesis of hierarchical BiVO₄/Bi₂O₂CO₃ nanocomposites with enhanced visible-light photocatalytic activity. *Appl. Catal. B* **2011**, *110*, 286–295. [[CrossRef](#)]
26. Liang, N.; Zai, J.T.; Xu, M.; Zhu, Q.; Wei, X.; Qian, X.F. Novel Bi₂S₃/Bi₂O₂CO₃ heterojunction photocatalysts with enhanced visible light responsive activity and wastewater treatment. *J. Mater. Chem. A* **2014**, *2*, 4208–4216. [[CrossRef](#)]
27. Huang, Y.; Fan, W.; Long, B.; Li, H.; Zhao, F.; Liu, Z.; Tong, Y.; Ji, H. Visible light Bi₂S₃/Bi₂O₃/Bi₂O₂CO₃ photocatalyst for effective degradation of organic pollutions. *Appl. Catal. B Environ.* **2016**, *185*, 68–76. [[CrossRef](#)]
28. Dong, F.; Li, Q.Y.; Sun, Y.J.; Ho, W.K. Noble metal-like behavior of plasmonic Bi particles as a cocatalyst deposited on (BiO)₂CO₃ microspheres for efficient visible light photocatalysis. *ACS Catal.* **2014**, *4*, 4341–4350. [[CrossRef](#)]
29. Xiong, T.; Huang, H.W.; Sun, Y.J.; Dong, F. In-Situ synthesis of a C-doped (BiO)₂CO₃ hierarchical self-assembly effectively promoting visible light photocatalysis. *J. Mater. Chem. A* **2015**, *3*, 6118–6127. [[CrossRef](#)]
30. Huang, H.W.; Xiao, K.; Yu, S.X.; Dong, F.; Zhang, T.R.; Zhang, Y.H. Iodide surface decoration: An facile and efficacious approach to modulating the band energy level of semiconductors for high performance visible-light Photocatalysis. *Chem. Commun.* **2016**, *52*, 354–357. [[CrossRef](#)] [[PubMed](#)]
31. Dong, F.; Li, Q.; Ho, W.; Wu, Z.B. The mechanism of enhanced visible light photocatalysis with micro-structurally optimized and graphene oxide coupled (BiO)₂CO₃. *Chin. Sci. Bull.* **2015**, *60*, 1915–1923.
32. Li, Q.; Liu, H.; Dong, F.; Fu, M. Hydrothermal formation of N-doped (BiO)₂CO₃ honeycomb-like microspheres photocatalysts with bismuth citrate and Dicyandiamide as precursors. *J. Colloid Interface Sci.* **2013**, *408*, 33–42. [[CrossRef](#)] [[PubMed](#)]
33. Liu, Y.; Wang, Z.; Huang, B.; Yang, K.; Zhang, X.; Qin, X.; Dai, Y. Preparation, electronic structure, and photocatalytic properties of Bi₂O₂CO₃ nanosheet. *Appl. Surf. Sci.* **2010**, *257*, 172–175. [[CrossRef](#)]

34. Chang, C.; Teng, F.; Liu, Z. Fully Understanding the Photochemical Properties of $\text{Bi}_2\text{O}_2(\text{CO}_3)_{1-x}\text{S}_x$ Nanosheets. *Langmuir* **2016**, *32*, 3811–3819. [[CrossRef](#)] [[PubMed](#)]
35. Huang, H.; Li, X.; Wang, J.; Dong, F.; Chu, P.K.; Zhang, T.; Zhang, Y. Anionic Group Self-Doping as a Promising Strategy: Band-Gap Engineering and Multi-Functional Applications of High-Performance CO_3^{2-} -Doped $\text{Bi}_2\text{O}_2\text{CO}_3$. *ACS Catal.* **2015**, *5*, 4094–4103. [[CrossRef](#)]
36. Zhao, Z.; Zhou, Y.; Wang, F.; Zhang, K.; Yu, S.; Cao, K. Polyaniline-Decorated {001} Facets of $\text{Bi}_2\text{O}_2\text{CO}_3$ Nanosheets: In Situ Oxygen Vacancy Formation and Enhanced Visible Light Photocatalytic Activity. *ACS Appl. Mater. Interfaces* **2015**, *7*, 730–737. [[CrossRef](#)] [[PubMed](#)]
37. Pawar, R.C.; Khare, V.; Lee, C.S. Hybrid photocatalysts using graphitic carbon nitride/cadmium sulfide/reduced graphene oxide (g- C_3N_4 /CdS/RGO) for superior photodegradation of organic pollutants under UV and visible light. *Dalton Trans.* **2014**, *43*, 12514–12527. [[CrossRef](#)] [[PubMed](#)]
38. Liu, G.; Chen, Z.; Dong, C.; Zhao, Y.; Li, F.; Lu, G.Q.; Cheng, H.-M. Visible Light Photocatalyst: Iodine-Doped Mesoporous Titania with a Bicrystalline Framework. *J. Phys. Chem. B* **2006**, *110*, 20823–20828. [[CrossRef](#)] [[PubMed](#)]



© 2018 by the authors. Licensee MDPI, Basel, Switzerland. This article is an open access article distributed under the terms and conditions of the Creative Commons Attribution (CC BY) license (<http://creativecommons.org/licenses/by/4.0/>).